Nanoscale

ROYAL SOCIETY OF CHEMISTRY

PAPER

View Article Online
View Journal | View Issue

Cite this: *Nanoscale*, 2023, **15**, 7991

Spatio-temporally deciphering peripheral nerve regeneration *in vivo* after extracellular vesicle therapy under NIR-II fluorescence imaging†

Yueming Wang,‡[a] Huaixuan Sheng,‡[b] Meng Cong,‡[c] Wenjin Wang,[d] Qianru He,[c] Huizhu Li,[b] Shunyao Li,[b] Jian Zhang,[b] Yuzhou Chen,[g] Shuaicheng Guo,[e,f] Lu Fang,[e,f] Stefano Pluchino,[h] Ewelina Biskup,[i,j] Mikhail Artemyev,[k] Fuchun Chen,[f] Yunxia Li,[b] Jun Chen,*[b] Sijia Feng*[b] and Yan Wo*[a]

Extracellular vesicles (EVs) show potential as a therapeutic tool for peripheral nerve injury (PNI), promoting neurological regeneration. However, there are limited data on the *in vivo* spatio-temporal trafficking and biodistribution of EVs. In this study, we introduce a new non-invasive near-infrared fluorescence imaging strategy based on glucose-conjugated quantum dot (QDs-Glu) labeling to target and track EVs in a sciatic nerve injury rat model in real-time. Our results demonstrate that the injected EVs migrated from the uninjured site to the injured site of the nerve, with an increase in fluorescence signals detected from 4 to 7 days post-injection, indicating the release of contents from the EVs with therapeutic effects. Immunofluorescence and behavioral tests revealed that the EV therapy promoted nerve regeneration and functional recovery at 28 days post-injection. We also found a relationship between functional recovery and the NIR-II fluorescence intensity change pattern, providing novel evidence for the therapeutic effects of EV therapy using real-time NIR-II imaging at the live animal level. This approach initiates a new path for monitoring EVs in treating PNI under *in vivo* NIR-II imaging, enhancing our understanding of the efficacy of EV therapy on peripheral nerve regeneration and its mechanisms.

Received 20th February 2023,
Accepted 29th March 2023

DOI: 10.1039/d3nr00795b

rsc.li/nanoscale

[a]*Department of Anatomy and Physiology, School of Medicine, Shanghai Jiao Tong University, Shanghai 200025, China. E-mail: yanwosh@163.com*
[b]*Sports Medicine Institute of Fudan University, Department of Sports Medicine, Huashan Hospital, Fudan University, Shanghai 200040, China. E-mail: biochenjun@fudan.edu.cn, sjfeng13@fudan.edu.cn*
[c]*Key Laboratory of Neuroregeneration of Jiangsu and Ministry of Education, Co-Innovation Center of Neuroregeneration, Jiangsu Clinical Medicine Center of Tissue Engineering and Nerve Injury Repair, Nantong University, Nantong, JS 226001, China*
[d]*Department of Plastic and Reconstructive Surgery. Shanghai ninth People's Hospital, Shanghai Jiao Tong University School of Medicine, Shanghai 200011, China*
[e]*University of Chinese Academy of Sciences, Beijing 100049, China*
[f]*Key Laboratory of Infrared System Detection and Imaging Technology, Shanghai Institute of Technical Physics, Chinese Academy of Sciences, Shanghai 200083, China*
[g]*Department of Othopedic Surgery, Xin Hua Hospital affiliated to School of Medicine, Shanghai Jiao Tong University, Shanghai 200092, China*
[h]*Department of Clinical Neurosciences, University of Cambridge, Cambridge CB2 0AH, UK*
[i]*Department of Basic and Clinical Science, Shanghai University of Medicine and Health Sciences, Shanghai 201318, China*
[j]*Department of Oncology, Renji Hospital, School of Medicine, Shanghai Jiao Tong University, Shanghai 200001, China*
[k]*Research Institute for Physical Chemical Problems of the Belarusian State University, Leningradskaya srt., 14, Minsk, 220006, Belarus*

†Electronic supplementary information (ESI) available. See DOI: https://doi.org/10.1039/d3nr00795b

‡These authors contributed equally to this work.

Introduction

The incidence of peripheral nerve injury (PNI) is approximately 13 to 23 per 100 000 persons per year,[1–3] leading to lifelong disorders including neural dysfunction, unbearable pain, paralysis and even permanent disability. Various treatment modalities such as nerve repair and neural transplantation have been employed for peripheral nerve regeneration for decades,[4–8] but these therapeutics result in only a 51.6% satisfactory recovery with slow nerve regeneration and incomplete recovery of neural function.[9] Especially, when nerve crush injury occurs, the current treatments mainly based on surgical procedures might ultimately lack scope for their abilities.

Recently, skin precursor (SKP) derived Schwann cells (SKP-SCs) have been applied to traumatic and degenerative neurological diseases. They are increasingly qualified as a favorable tool in neuroregenerative medicine, demonstrating improved functional recovery in rats with acute and delayed PNI.[10–12] It has gradually become evident that SKPs exploit extracellular vesicles (EVs) of 40 nm to 1000 nm in size secreted into extracellular fluids, as a paracrine communication mechanism to augment endogenous neuroprotection and improve neurological impairment.[13] In recent years, EVs

have been extensively investigated in the field of peripheral nerve regeneration due to their ability to transfer cargos among cells and regulate their activities, exerting regenerative effects on neurological impairment with assorted mechanisms involved in neurogenesis, neuronal proliferation, neuronal survival, neurogenesis, and angiogenesis.[14–19] Furthermore, as EVs are biogenic in nature and in the absence of immunostimulatory activity owing to their biological origin with prime physicochemical stability, they are typically endowed with superior tolerance compared to synthetic drugs. In particular, it was reported that SKP-SCs derived EVs (SKP-SC-EVs) could regulate cell growth and the death signaling pathway through cargo transmission to injured motoneurons, contributing to axonal regrowth and neuronal resurrection.[20] Based on accumulating evidence for the key role of EVs in neuronal protection, nerve regeneration, remyelination, and synaptic plasticity,[21–24] a cell-free therapeutic therapy based on SKP-SC-EVs can be postulated as a promising candidate for the treatment of PNI without indication for surgery.

As the EV therapy is expected to be a novel potential for optimizing peripheral nerve regeneration in the treatment of PNI, it is crucial to understand when, where and how the EVs exert their therapeutic effect. However, the migration time, spatial distribution, and retention of EVs *in vivo*, which are closely related to the effectiveness and efficacy of EV therapy, during peripheral nerve regeneration remain unknown due to a lack of real-time monitoring modalities. Moreover, non-invasive analysis and prediction of functional recovery in the course of treatment are anticipated for timely adjustment of EV administration. Hence, there is an urgent need for a reliable *in vivo* imaging method to quantitatively assess the efficacy of EV therapy on peripheral nerve regeneration and to guide EV administration for functional recovery in the treatment of PNI.

In recent years, nanotechnologies have contributed to advances in *in vivo* high-resolution imaging to study stem cells and EV tracking and homing, providing novel insights into their mechanisms of action.[25–27] Notably, fluorescence imaging is becoming one of the most widely utilized techniques in the field of medical science. The second near-infrared window (NIR-II, 1000–1700 nm) fluorescence imaging has made its debut by virtue of minimal scattering, high signal-to-noise ratio (SNR) and low self-fluorescence background compared with visible light and NIR-I fluorescence imaging.[28–32] Among various NIR-II imaging agents, lead sulfide quantum dots (PbS QDs) have been adopted to track stem cells and monitor their fate during rotator cuff repair.[33] Moreover, nerve regeneration after PNI has been demonstrated after surgical repair combined with injection of adipose tissue derived stem cells (ADSCs), simultaneously providing long-term and real-time details on the distribution, migration and clearance of the injected cells.[34] Inspired by these previous discoveries, the application of QD-based NIR-II fluorescence imaging may hopefully serve as an excellent strategy for monitoring EVs *in vivo* dynamically and longitudinally in real-time. Furthermore, previous studies found that glucose-coated nanoparticles were uptaken into EVs *via* an active energy-dependent mechanism that is mediated by the glucose transporter GLUT-1.[35,36] Therefore, glucose-coated quantum dot (QDs-Glu) labeling could be a novel path to unveil the relationship between the therapeutic effects of EV therapy and a possible illustration of the spatio-temporal changing pattern of EVs *in vivo* in a non-invasive and real-time manner, generating a noteworthy potential for deciphering the underlying mechanisms for peripheral nerve regeneration and predicting neurofunctional recovery.

In the present work, an innovative approach for EV labeling that preserves their morphology and physiological characteristics and longitudinal monitoring of EVs *in vivo* was performed, providing a spatio-temporal map of EVs and allowing for in-depth interpretation of nerve regeneration after EV therapy (Scheme 1). First, our prepared QDs were conjugated to glucose (QDs-Glu), which acted as an effective target for QDs to label rat SKP-SC-EVs obtained and expanded *in vitro* and to track them *in vivo*. Then, the fluorescence properties and stability of QD-labeled EVs (QDs-Glu-EVs) were studied both *in vitro* and *in vivo*. Subsequently, a cell-free therapy research platform based on EVs was constructed, which was applied to the crushed nerves in rat models of sciatic nerve injury, with NIR-II fluorescence recorded in a time course *in vivo*. Furthermore, the therapeutic effects of EV therapy were verified through immunofluorescence and behavioral tests, evaluating axonal outgrowth and regrowth as well as motor and sensory recovery. Additionally, pathological analysis was employed to testify the biosafety of QDs-Glu-EVs. The current work proved peripheral nerve regeneration after the EV therapy and provided long-term and real-time details through NIR-II fluorescence imaging on the fate of injected EVs, verifying their therapeutic effects in the treatment of PNI and an overall interpretation of functional recovery at the living level, paving the way for future clinical applications of EV therapy.

Materials and methods

Reagents and materials

Chemical reagents, including bovine pancreatic ribonuclease-A (RNase-A), lead acetate trihydrate ($Pb(OAc)_2{\cdot}3H_2O$), sodium sulfide nonahydrate ($Na_2S{\cdot}9H_2O$), *N*-hydroxysuccinimide (NHS),and D-(β)-glucosamine hydrochloride (2GF) were purchased from Sigma-Aldrich, and 1-ethyl-3-(3-dimethylaminopropyl) carbon diimine hydrochloride (EDC) and Sulfo-SMCC were purchased directly purchased from Thermo Fisher Scientific, and used without further purification. Additionally, 97% sodium hydroxide (NaOH) obtained from Maclin and sterile 1× phosphate buffer solutions (PBS) with a pH of 7.4 were employed in all experiments.

Animals

All the experimental animals including 6- to 8-week-old female Sprague-Dawley (SD) rats (weight: around 180 g) and 6- to 8-week-old female nude mice were provided by the Animal Care Facility of Shanghai Jiao Tong University, School of

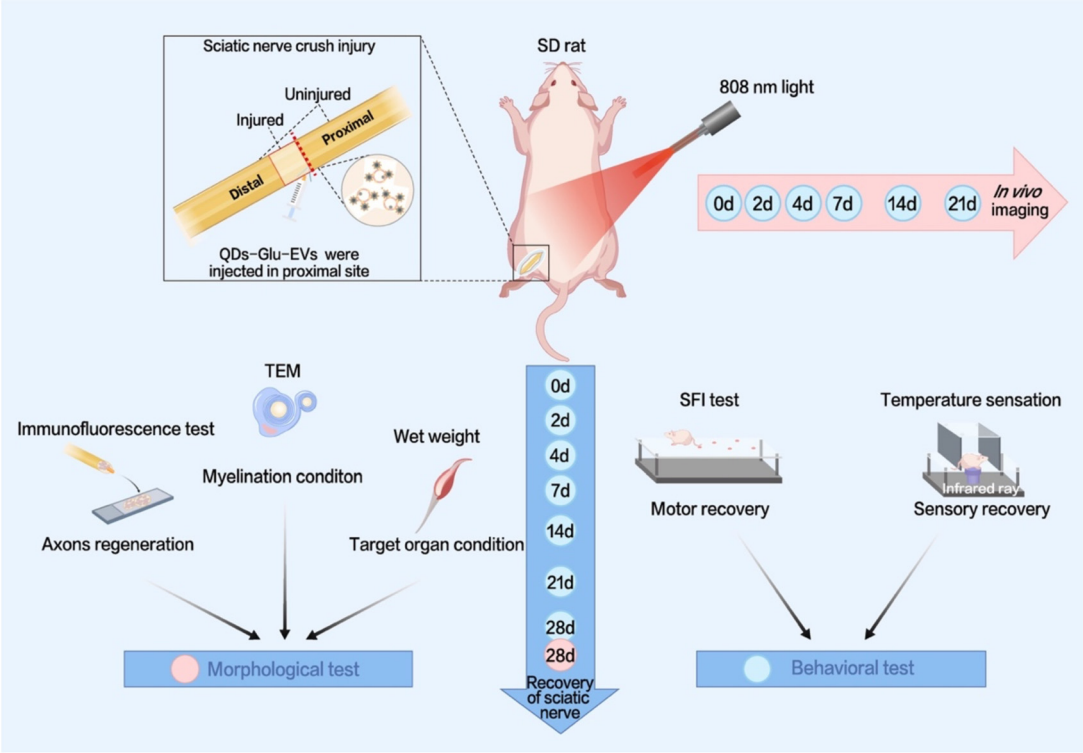

Scheme 1 Schematic of the experimental process.

Medicine (Shanghai, China). All animal experiments were carried out under aseptic conditions after the rats were anesthetized by isoflurane inhalation. The animal study protocols were performed according to the Chinese Guidelines for the Care and Use of Laboratory Animals and approved by the Animal Care Committee of the Laboratory Animal (201903001S).

Instrumentation

Deionized water was obtained using an ELGA Purelab classic ultraviolet filter system. The cultured EVs were observed using a Leica TCS SP8 microscope. Animal model establishment was performed under a SMOIF SXP-1C microscope. A biosafety cabinet of 1300 SERIES A2 from Thermo SCIENTIFIC was used. PbS quantum dots were produced using a Discover microwave reactor (CEM, USA) equipped with a cooling system. After synthesis, ultracentrifugation with Amicon ultra centrifugal filter tubes (MWCO: 10 kDa) was conducted to refine the PbS quantum dots. An NS1 NanoSpectralyzer fluorimetric analyzer was used to measure NIR-II fluorescence spectra of the PbS quantum dots, with an excitation wavelength of 808 nm. To capture NIR-II fluorescence images, an *in vivo* imaging system (MARS, Artemis Intelligent Imaging, Shanghai, China) was employed. A fiber-coupled 808 nm laser was used as the excitation source, providing shadowless illumination. A 1250 nm long-pass filter was used to filter the emitted light, which was then collimated using a 50 mm focal length SWIR lens (MARS-FAST, Artemis Intelligent Imaging, Shanghai, China). The fluorescence was detected using a NIRvana 640 liquid-nitrogen-cooled InGaAs camera (Teledyne Princeton Instruments) positioned vertically above the working stage to irradiate the subject.

Synthesis of PbS QDs

The procedure for synthesizing PbS quantum dots was based on a previously published paper.[37] Initially, a solution of Pb $(OAc)_2$ (10 mM) and RNase-A (50 mg mL^{-1}) was mixed to obtain the RNase-A/Pb^{2+} solution, which was then added to a reaction tube. The pH of the system was adjusted to 9–11 by stirring the mixture with 50 μl of NaOH solution (1 M) for 5 minutes. Subsequently, 50 μl of freshly prepared Na_2S solution (10 mM) was added, and the mixture was stirred with a stir bar to ensure even heating before being inserted into the microwave reactor. The solution turned into a transparent dark brown when the PbS quantum dots were freshly prepared. Finally, the solution was purified using ultrafiltration and rinsed with PBS to remove any excess reagents. The prepared PbS quantum dots were stored in the dark at 4 °C after synthesis.

Culture of SKPs and differentiation towards SCs

Rats at postnatal day 1 were used for primary culture of SKPs as described previously.[38] Briefly, back skin samples from neonatal SD rats were cut into 1–2 mm^2 pieces, followed by careful removal of tissue underlying the dermis. Skin tissue was digested with 0.1% trypsin or 1 mg mL^{-1} collagenase for 45–60 min at 37 °C, and then mechanically dissociated, followed by filtration through a 40 μm cell strainer. The cells were

plated at a density of (1–2.5) × 10^4 cells per mL in Dulbecco's modified Eagle's medium (DMEM)/F12 medium (Corning Cellgro, Manassas, VA, USA) containing 0.1% penicillin/streptomycin (Beyotime, Shanghai, China), 40 ng mL^{-1} fibroblast growth factor 2 (FGF2; R&D System, Minneapolis, MN, USA), 20 ng mL^{-1} epidermal growth factor (EGF; R&D), and 2% B27 supplement (Gibco, Brooklyn, NY, USA), with a 1–2 mL medium containing sufficient supplements was added every 3 days. For differentiation towards SCs, SKP spheres were dissociated and cultured on plates coated with poly-D-lysine (PDL; Sigma-Aldrich, St Louis, MO, USA) and laminin (Corning, Brooklyn, NY, USA) in SKP-SC differentiation medium I, namely DMEM/F12 medium containing 0.1% penicillin/streptomycin, 40 ng mL^{-1} FGF2, 20 ng mL^{-1} EGF, 2% B27 supplement, and 5–10% fetal bovine serum (FBS; Gibco, Carlsbad, CA, USA). After 3 days, the medium was changed to SC differentiation medium II, namely DMEM/F12 (3 : 1) containing 0.1% penicillin/streptomycin, 5 μm of forskolin (Sigma-Aldrich, St Louis, MO, USA), 50 ng mL^{-1} heregulin-1β (R&D), 2% N2 supplement (StemCell Technologies, Vancouver, BC, Canada), and 1–5% FBS. Once the proliferating SCs showed an identifiable morphology, the cell colonies were isolated and cultured in SC proliferation medium (the same as SC differentiation medium II) for passage culture.

Isolation and identification of SKP-SC-EVs

First, the EVs released from SKP-SCs were isolated. The SKP-SCs were incubated in the proliferation medium without FBS for 2 days at about 80% confluence (cell density). The harvested conditioned culture medium was centrifuged at 500*g* for 10 min, followed by collection of the supernatants. EVs were purified from the cell culture supernatant of SKP-SCs that were cultured in differentiation medium. After the cell density reached 80% confluence, the medium was switched to serum-free medium for 48 h. The supernatant, namely conditioned medium, was collected and went through sequential ultracentrifugation at 500*g* for 10 min to remove the cell debris, followed by filtering through a 0.22 μm filter (Millipore). EVs were isolated using the exoEasy kit (Qiagen, Germantown, MD, USA) from 15 mL of the cell culture supernatant with detailed experiment steps in the manufacturer's protocol. The morphology of the EVs was observed under a transmission electron microscope (TEM, Hitachi, Tokyo, Japan), and nanoparticle tracking analysis (NTA, Particle Metrix, Ammersee, Germany) was utilized to measure the concentration and size distribution of SKP-SC-EVs. The protein concentration was measured using bicinchoninic acid (BCA) protein assay (Thermo Scientific), and exosomal markers CD9, CD63, and CD81 as well as tumor susceptibility gene 101 (TSG101) were detected by western blot analysis.

EV labeling by QDs-Glu

The pH of the PbS QD solution was adjusted to 5–6 using NaOH and HCl. 0.24 mg of EDC and NHS were added into 1 mL of PbS QD solution, and the mixture was vibrated at room temperature for 40 min. 0.175 mg of glucose-2 (2GF) was added to the mixture.[39] After the overnight reaction at 4 °C, the mixture was centrifuged using an ultrafiltration tube to remove the unbound free impurities. Then, the EVs were co-incubated with QDs-Glu overnight at 4 °C.

Preparation of experimental animal models

After at least 1 week of habituation, SD rats were randomized for the experimental group and surgical procedures were performed under isoflurane anesthesia (3% induction and 2% maintenance) with the rats placed properly in the prone position. The left sciatic nerve was exposed just below the sciatic notch under sterile conditions and then crushed using Dumont #5/45 forceps for 30 s under a microscope. After the nerve injury, the incision was closed and sterilized, and the rats were allowed to recover on heated pads before being returned to their home cage.

In vivo observation

The rats were anesthetized by isoflurane inhalation and fixed in the prone position for NIR-II imaging. 10 μl of the QDs-Glu-labeled EVs at different concentrations (5 × 10^7, 2.5 × 10^7 and 5 × 10^6 EVs) were first injected subcutaneously on the back for observation. The control group was treated with the same volume of PBS. Next, the QDs-Glu-labeled EVs were injected in sciatic nerve injury models. After the crushed sciatic nerve was exposed, 10 μl of the QDs-Glu-labeled EVs (5 × 10^7 EVs) were injected into the proximal side of the injured nerve. An NIR-II fluorescence imaging system was then used to observe the migration of the injected EVs with images taken in a time course (0 d, 2 d, 4 d, 7 d, 14 d and 21 d post-injection). The PL intensity was measured from the site of the injury of collected NIR-II images using Fiji.

Immunofluorescence staining

To determine cell survival, axonal regeneration and myelination by the transplanted cells, nerve tissue including distal to the repair site was harvested after 28 days with samples fixed in 4% paraformaldehyde (PFA) (Beyotime, Shanghai, China) at room temperature (RT) for 15 min and then washed 3 times with PBS. Next, the cells were closed with the blocking solution (Beyotime) at RT for 1 h, and then incubated with the primary antibody at 4 °C overnight, followed by incubation with the secondary antibody at RT in the dark for 2 h. Finally, the cells were counterstained with 4′,6-diamidino-2-phenylindole (DAPI) (Sigma-Aldrich, MO, USA), and the photomicrographs were taken using a confocal microscope (SP5, Leica, Mannheim, Germany). Schwann cells were labeled with anti-S100β, nerve fibers were labeled with anti-NF200, and nuclei were stained with DAPI.

Toluidine blue staining

After functional and behavioral tests were completed, a 0.5 cm-long piece of the sciatic nerve at the 1 cm distal end of the lesion was separated and removed from the rats (n = 4 per group). The nerves were then sliced into 5 μm-thick cross-sections. The segments were stained with 1% toluidine blue at

room temperature for 30 min, washed gently in water, and consecutively soaked in 95% ethanol and 100% ethanol for 2–3 s. Images were acquired at 400× magnification using a dissecting microscope. The axon and fiber diameters were measured using Image J software. The myelin thickness and *g*-ratio were calculated as follows: myelin thickness = (fiber diameter − axon diameter)/2. *G*-Ratio = axon diameter/fiber diameter.

Hematoxylin and eosin staining

The sciatic nerves were dissected and postfixed overnight after 28 days. Samples were embedded in paraffin and sectioned at 8 μm. Slides were washed in xylene for 5 min followed by two washes in 100% ethanol (5 min) and 95% ethanol (2 × 5 min). Tissues were then dipped in distilled water for 2 min and immersed for 10 min in Harris hematoxylin. After that the sections were differentiated in 1% acid alcohol for 30 s, quickly washed with water for 1 min, and blued in 0.2% ammonia water for 30 s before a 3 min rinse in tap water. After that the sections were quickly immersed in 95% ethanol (1 min) and stained with eosin solution for 1 min. The slides were then dehydrated by successive incubations in 95% ethanol, 100% ethanol and xylene (two incubations of 4 min at each step) and mounted using cytosol. Images were captured with a NIKON ECLIPSE 80i microscope and a NIKON DS-Qi1MC camera (4×) using NIS-Elements AR 3.10 software.

Transmission electron microscopy

Sections of the regenerated nerves were fixed in precooled 2.5% glutaraldehyde for 3 h followed by postfixation in a 1% osmium tetroxide solution for 1 h, washed, dehydrated, embedded in Epon 812 epoxy resin, cut into ultrathin sections at 60 nm, and stained with lead citrate and uranyl acetate. The stained sections were observed under a transmission electron microscope (JEM-1200, JEOL Ltd, Tokyo, Japan).

Wet weight rate of the gastrocnemius muscle

Gastrocnemius muscles were collected from both the injured and uninjured sides after 28 days. Blood vessels and the deep fascia covering the surfaces of the muscle were removed and discarded. The gastrocnemius muscles were then weighed. The wet weight rate was calculated using the following equation: the wet weight rate of the gastrocnemius muscle = wet weight of the injured muscle/wet weight of the uninjured muscle.

Behavioral tests

All behavior experiments were conducted in a blinded fashion in a quiet room (temperature 22 °C ± 1 °C) from 9 AM to 6 PM. For motor recovery, the sciatic functional index (SFI) was calculated. Briefly, the rats were trained to walk across a custom-made walking box (100 cm long, 12 cm wide, and 10 cm high), leading to a darkened box. White paper (12 cm × 100 cm) lined the bottom of the track. The rats' hind paws were dipped in red dye before it walked the track at each timepoint. Each rat was then allowed to walk the track three or four times until five measurable footprints were collected. The length between the third toe and the heel (PL), the first and fifth toes (TS), and the second and fourth toes (ITS) were measured on the experimental side (EPL, ETS, and EITS, respectively) and the contralateral normal side (NPL, NTS, and NITS, respectively). Then, the SFI was measured and calculated using the following formula: SFI = (−38.3 × (EPL − NPL)/NPL) + (109.5 × (ETS − NTS)/NTS) + (13.3 × (EIT-NIT)/NIT) − 8.8. A plantar test apparatus was used to assess heat hyperalgesia. The forepaw withdrawal latency responding to heat stimulation (Woodland Hills, CA, USA) was measured.[40] Testing was performed using a blind performer. Assessments were made including baseline and different time points after treatment. The baseline values of paw withdrawal were calculated by an average of 4 consecutive withdrawal latencies of injured hind paws detected at 15 min intervals. The completion of each test may be indicated either by the sudden withdraw of the paw or lick the leg.

Statistical analysis

Statistical analyses were performed with Graph Pad Prism 8.0. All values are expressed as the mean ± SD. Two-tailed unpaired Student's *T*-test was used to compare a single measurement between two groups. One-way ANOVA followed by Dunnett's multiple comparisons *post-hoc* test was used for time course analysis of a single group. Two-way ANOVA followed by Sidak's multiple comparison *post-hoc* test was used for the analyses of time course experiments comparing two groups. In all tests, *P*-value <0.05 was considered statistically significant.

Results and discussion

The schematic demonstrating the synthesis of QDs-Glu, isolation and labeling of SKP-SC-EVs and internalization by 293T cells is shown in Fig. 1a. The QDs were first prepared according to the previous protocol.[37] Then, the as-prepared QDs were conjugated to glucose (GLUT-1) forming QDs-Glu using the EDC–NHS method.[41] After co-incubated with SKP-SC-EVs isolated from SKP-SCs overnight, the QDs-Glu-EVs were successfully prepared.

Characterization of QDs-Glu-EVs, SKP-SC-EVs and QDs-Glu was performed to verify their morphological and physicochemical properties. Transmission electron microscopy (TEM) and dynamic light scattering (DLS) were used to study the size and shape of QDs-Glu-EVs in comparison with the other two. As shown in Fig. 1b1, the QDs-Glu accumulated and formed a spherical structure alongside with the membrane of EVs, comparing to pure Glu-QDs and pure SKP-SC-EVs (Fig. 1b2 and b3). The data of DLS showed that the average size of QDs-Glu-EVs was around 166.5 nm compared with SKP-SC-EVs of around 161.6 nm and QDs-Glu of 100.9 nm (Fig. 1c1–c3). For further evidence, the zeta potentials of QDs-Glu-EVs, SKP-SC-EVs and QDs-Glu were recorded and compared. As shown in Fig. 1d1–d3, the original SKP-SC-EVs had a surface potential of −17.9 mV and QDs-Glu had a surface potential of −1.54 mV, which could result from the negatively charged chemical groups in the protein ligand such as carboxyl or hydroxyl. In comparison, QDs-Glu-EVs showed a zeta potential

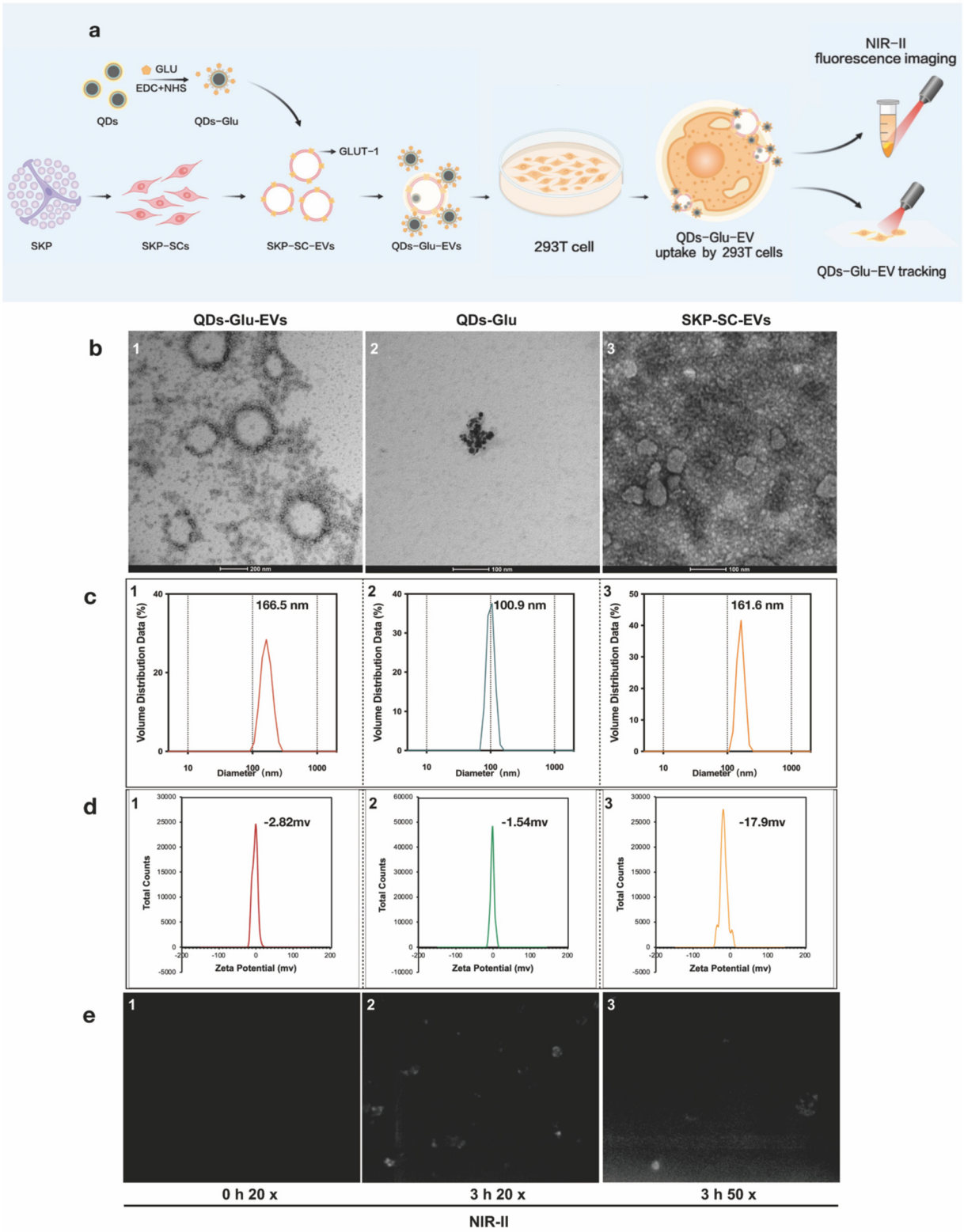

Fig. 1 Preparation and characterization of QDs-Glu-EVs. (a) Schematic of the synthesis of QDs-Glu and labeling of SKP-SC-EVs. (b1–b3) TEM images, (c1–c3) DLS measurement and (d1–d3) Zeta-potential measurement of SKP-SC-EVs, QDs-Glu and QDs-Glu-EVs. (e1–e3) Internalization of QDs-GLU-EVs by 293T cells under NIR-II fluorescence imaging (λ_{ex}: 808 nm, exposure time: 50 ms).

of −2.82 mV. The changing of the surface charge indicated the interaction occurring in the process of uptake.

Additionally, whether the QDs-Glu-EVs with robust fluorescence properties and stability could be transferred to 293T cells was examined (Fig. S1†). After co-culture with 293T cells for 3 h–12 h, the morphology of 293T cells with QDs-Glu-EVs showed no obvious abnormality, indicating the internalization of EVs by motoneurons as expected (Fig. S2†). Moreover, the NIR-II fluorescence signals inside the EVs observed at 3 h of co-culture also suggested that the internalization functions of EVs were well preserved after labeling (Fig. 1e1–e3). This could also be applied to validate the endocytosis and exocytosis effects during *in vivo* observation and the biosafety of QDs-Glu when labeling EVs.

In summary, NIR-II fluorescence imaging based on QDs-Glu demonstrated favorable fluorescence properties and is capable of labeling EVs *in vitro*. These results suggested that EVs preserved their morphology and physiological characteristics after labeling, and QDs-Glu had promising potential for tracking EVs *in vivo*, achieving real-time migration, distribution and retention data of EVs.

The fluorescence properties of QDs-Glu-EVs compared with QDs-Glu were verified and are in Fig. 2. As shown in Fig. 2a, NIR-II fluorescence images of 1 mL of QDs-Glu-EVs and 100 μl of QDs-Glu were obtained with an excitation wavelength of 808 nm under increasing exposure time (1 ms, 3 ms, 5 ms, 7 ms, 10 ms and 15 ms). The solution of QDs-Glu could be clearly observed even at a short exposure time of 1 ms, with an increasing PL intensity from 1 ms to 3 ms and remaining high from 3 ms to 15 ms (Fig. 2b), confirming the excellent fluorescence intensity and sensitivity of this imaging agent as reported in the previous studies.[33,37] On the other hand, it was shown that the PL intensity of QDs-Glu-EVs increased steadily from 1 ms to 15 ms and reached the same level as that of QDs-Glu, indicating that exposure time over 15 ms should be adopted for the fluorescence signals to be maximized during the observation. Furthermore, the normalized PL spectra of both QDs-Glu and QDs-Glu-EVs shared a similar emission peak at around 1300 nm, locating within the range of NIR-II window (Fig. 2c). Interestingly, a slight red shift of the peak of QDs-Glu-EVs was discerned compared to that of QDs-Glu, which could be attributed to the growing size of a QD–protein composite after uptake by EVs with a smaller interplanar spacing of the crystalline structure.[42–48] This phenomenon could be further verified by the NIR-II fluorescence images under a microscope. As shown in Fig. 1e, fluorescence signals were detected from the EVs showing fluorescent dots, which should be the accumulated QDs-Glu uptake by EVs after co-culture for 3 h.

Despite the effectiveness of labeling EVs by QDs-Glu *in vitro*, further validation of the sensitivity and stability of labeled EVs *in vivo* was required. As shown in Fig. 2d, three concentrations of QDs-Glu-EVs (5×10^7, 2.5×10^7 and 5×10^6 EVs) and PBS (pH = 7.4) compared with QDs-Glu were subcutaneously injected into four different sites on the dorsum of a nude mouse with NIR-II images recorded in a time course (0 d, 7 d, 14 d, 21 d and 28 d post-injection). Overall, the fluorescence signals decreased gradually at the four points with injected QDs-Glu-EVs and QDs-Glu as the observation time increased. It was demonstrated that the NIR-II imaging system was able to visualize as low as 5×10^6 EVs and fluorescence signals could only be detected at the first two points with 5×10^7 EVs and 2.5×10^7 EVs at 28 d post-injection. Specifically, the injection site with the highest EVs concentration (5×10^7 EVs) showed the highest fluorescence signals for the longest time, demonstrating that EVs could be best detected at this concentration using the NIR-II imaging system. Furthermore, the corresponding PL intensity was measured from Fig. 2d at 0 d post-injection, which exhibited a linear relationship with the EV concentration (Fig. 2e). Moreover, the area and PL intensity measured from the four injection points on Fig. 2d were shown in Fig. 2e–f, in accordance with the fluorescence signals. These results confirmed again that the QDs-Glu-EVs were successfully labeled and could be tracked *in vivo* with high sensitivity and stability.

Thus, desirable sensitivity and stability of QD-based NIR-II imaging both *in vitro* and *in vivo* proved that it was promising for visualization and monitoring of the long-time translocation of EVs for medical applications *in vivo*. As the concentration of EVs capable of taking effects *in vitro* was reported to be approximately 10^8 EVs per mL,[49] then 5×10^7 EVs (10 μl of 5×10^9 EVs per mL) were chosen for the subsequent EV therapy *in vivo* to ensure therapeutic concentration of EVs in the injured nerve tissues.

The schematic of *in vivo* monitoring of EVs based on NIR-II fluorescence imaging is shown in Fig. 3a. SKP-SC-EVs were first labeled with QDs-Glu *in vitro* to prepare QDs-Glu-EVs with biosafety and the internalization ability was confirmed. After the sciatic nerve of the rat was exposed and crushed in the middle (Fig. S3†), 5×10^7 of QDs-Glu-EVs were injected into the proximal section of the injured nerve (Fig. 3b1) compared with pure QDs-Glu injection (Fig. 3c1). Then, longitudinal observation of the same area of interest by NIR-II imaging was initiated, with NIR-II fluorescence images obtained in a time course (0 d, 2 d, 4 d, 7 d, 14 d and 21 d post-injection).

Strong NIR-II fluorescence signals were clearly detected at both the proximal and distal sections of the crushed sciatic nerve at 0 d post-injection in both the QDs-Glu-EV and the QDs-Glu groups (Fig. 3b2 and c2). This indicated that most of the injected QDs-Glu-EVs and QDs-Glu were instantly excessive in the injection site covering both proximal and distal sections at first. Then, in the QDs-Glu-EV group, the fluorescence signals remained detectable and moved gradually from the proximal and distal sections (both ends) to the crushed site of the nerve (the center) throughout the 21-day observation, suggesting the migration of EVs from the uninjured site to the injured site of the nerve (Fig. 3b2–b7). In particular, the tendency to gather at the injured site turned most obvious from 4 d to 7 d post-injection, which suggested a release of contents from EVs, exerting a therapeutic effect on the injured nerve.[50,51] In contrast, the fluorescence signals in the QDs-Glu group remained at the same site after injection and decreased steadily around the injection site without obvious change of the location (Fig. 3c2–c7).

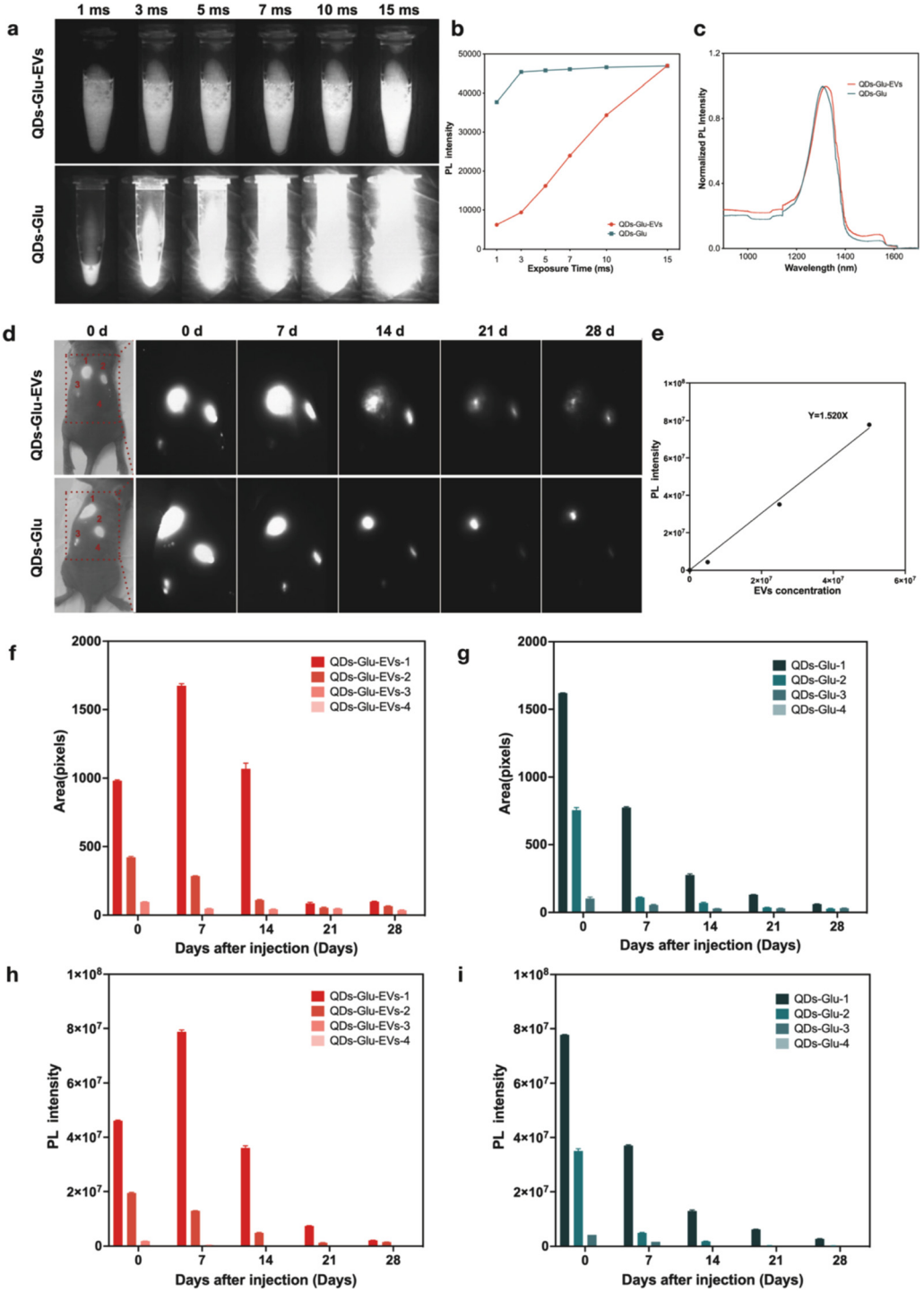

Fig. 2 Validation of the sensitivity and stability of QDs-Glu-EVs *in vitro* and *in vivo*. (a) NIR-II fluorescence images (λ_{ex}: 808 nm, exposure time: 1 ms, 3 ms, 5 ms, 7 ms, 10 ms and 15 ms), (b) PL intensity and (c) normalized PL spectra of QDs-Glu-EVs and QDs-Glu. (d) NIR-II fluorescence images of QDs-Glu-EVs (5×10^7, 2.5×10^7 and 5×10^6 EVs) and PBS injected subcutaneously in a nude mouse in a time course (0 d, 7 d, 14 d, 21 d and 28 d post-injection). (e) The linear relationship between the PL intensity measured from (d) and the concentration of injected EVs. (f–i) The area and PL intensity measured from the four injection points on (d).

Specifically, about the location of NIR-II fluorescence signals, the signals first appeared at both ends of the region of interest, which indicated the distribution of EVs at the initiation of the EV therapy. Then, the change of the signal location from the uninjured site to the injured site suggested the migration of EVs as drug vehicles for intercellular communication and for the transfer of materials including proteins, nucleic acids and even synthetic therapeutic agents.[52]

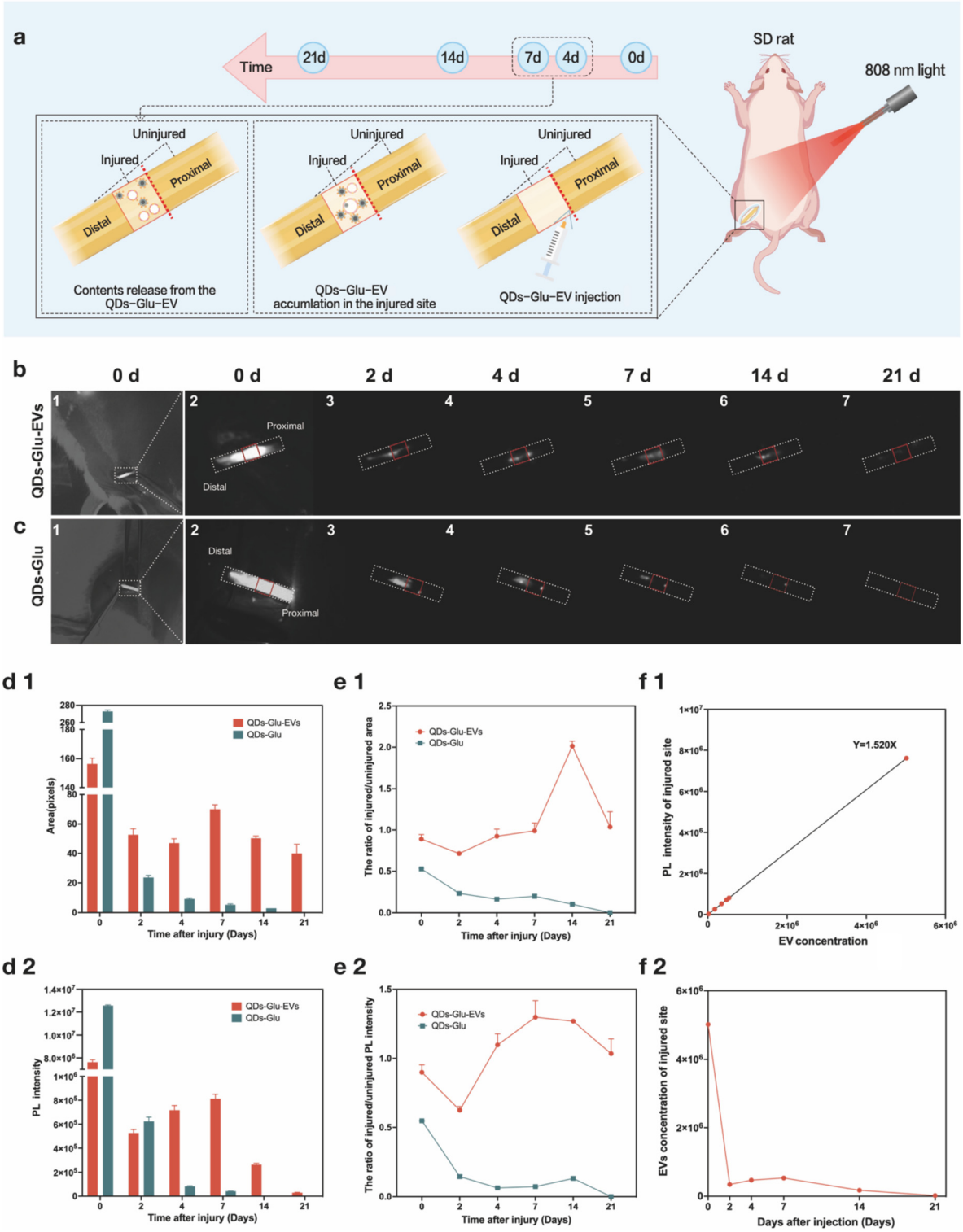

Fig. 3 *In vivo* monitoring of EVs based on an NIR-II fluorescence imaging strategy in rat models of sciatic nerve injury. (a) Schematic illustration of the *in vivo* monitoring of EVs. Bright field photograph of the region of interest and NIR-II fluorescence images (λ_{ex}: 808 nm, exposure time: 200 ms) of (b1–b7) the QDs-Glu-EV group compared with (c1–c7) the QDs-Glu group in a time course (0 d, 2 d, 4 d, 7 d, 14 d and 21 d post-injection). Mean (d1) fluorescence area and (d2) PL intensity of the injured nerve section, and the ratio of (e1) the fluorescence area and (e2) the PL intensity of uninjured/injured nerve sections between the QDs-Glu-EV group and the QDs-Glu group. (f1) Concentration of EVs *in vivo* calculated and conversed from the PL intensity based on Fig. 2e and (f2) estimated in a time course.

Finally, the fluorescence signals lasted for 21 days, showing the retention of EVs in the injured site with therapeutic effects. On the other hand, no obvious change of fluorescence signals was detected in the QDs-Glu group, which further verified that pure QDs-Glu not encapsulated in the EVs would not display a dynamic migration pattern but was gradually metabolized *in situ*. The comparison indicated that the EVs with active motion would migrate with an increase in time, thus resulting in a change in the location of fluorescence signals. It is worth noting that the nerve healing process leads to the release of numerous chemokines to promote nerve regeneration.[53] Therefore, it was postulated that chemotactic factors released during nerve regeneration might guide the migration of EVs to the injured site, where the Wallerian degeneration began and the regeneration would gradually initiate.[54,55]

To quantitatively evaluate the migration, distribution and retention of the injected EVs, the mean fluorescence area and the PL intensity in the injured section of the nerve were measured and are in Fig. 3d1 and d2. Compared with the QDs-Glu group with a constant decrease, the PL intensity and fluorescence area of the QDs-Glu-EV group decreased at first and then increased, followed with a decrease afterwards. It was indicated that the injured section was saturated with excessive EVs when first injected, which were then metabolized, showing a decrease in the concentration. Notably, the injected EVs from the uninjured sections gradually migrated to the injured section at 4 d to 7 d post-injection, causing an increase in the PL intensity and fluorescence area, and again were metabolized along with time. To demonstrate the result more clearly, the ratios of the injured/uninjured fluorescence area and the PL intensity of both groups were calculated and are presented in Fig. 3e1 and e2, the increasing ratio revealed an accumulation of EVs in the injured section of the nerve accompanied by reduction in the uninjured section (where the cells were initially injected) of the QDs-Glu-EV group in comparison with the QDs-Glu group. Additionally, as shown in Fig. 3f1, the *in vivo* EV concentration was calculated and conversed through the PL intensity according to Fig. 2e, based on which the *in vivo* EV concentration was estimated in a time course (Fig. 3f2). It was shown that the EV concentration increased from 2 d to 7 d and decreased from 7 d to 21 d post-injection, demonstrating a wave pattern with a peak at 7 d post-injection. Notably, this result was in accordance with the previous results that the EVs first migrated from the uninjured site to the injured site, causing an increase in the concentration and reaching a peak along with the release of contents. After that, the EVs could follow a fate of being broken and metabolized, leading to a gradual decrease in the concentration.

These results were believed to have shown that a spatio-temporal pattern of EVs in rats with sciatic nerve injury was visualized by QDs based NIR-II imaging *in vivo*. On this basis, it was reasonable to regard QDs as a candidate for monitoring the pharmacokinetics of EV therapy in peripheral nerve regeneration in clinical practice in future.

Pathological analysis based on immunofluorescence staining (neurofilaments in green and S100 in red) of the injured sciatic nerve from rats with (the QDs-Glu-EV group) (Fig. 4a) and without (the QDs-Glu group) (Fig. 4b) EV therapy was conducted at 4 weeks post-injection. Immunofluorescence histopathological analysis demonstrated a normal nerve fiber morphology in both groups with an insignificant difference in the number of nerve fibers per field, proving the occurrence of nerve regeneration after crushed injury (Fig. 4c). However, the QDs-Glu-EV group showed a significantly higher percentage of the S100 positive SCs ($P = 0.0421$) and muscle wet weight ($P = 0.0152$), which implied significantly superior nerve regeneration after the EV therapy (Fig. 4d and e).

In both preclinical and clinical settings, pathologic myelin abnormalities are often identified by studying the myelin ultrastructure. Hence, toluidine blue (TB) staining and TEM of nerve cross sections were performed to achieve qualitative and quantitative assessments of the sciatic nerve, enabling visualization of the morphology, the number of axons and the degree of myelination. The TB staining displayed less necrotic debris in the QDs-Glu-EV group (Fig. 4f1) than the QDs-Glu group (Fig. 4f5), confirming the therapeutic effects of EV therapy on nerve regeneration. As shown in Fig. 4f2–f4 compared with Fig. 4f6–f8, a more regular and organized morphology of myelin was shown in the QDs-Glu-EV group, along with a significantly larger average diameter of the myelinated nerve fiber ($P < 0.0001$) and myelin ($P < 0.0001$) (Fig. 4g and h). Specifically, the *G* ratio (axonal diameter/outer diameter of the whole nerve fiber) was adopted as a metric for the relative thickness of the myelin sheath in the cross-sectional micrographs, which was significantly lower ($P = 0.0254$) in the QDs-Glu-EV group (Fig. 4i). It is well-known that myelination of nerve fibers occurs during the regeneration of injured nerve fibers in an individual's lifetime (remyelination). The relationship between Schwann cells and axon directly influences the conduction velocity of the nerve fiber. An increase in the axonal diameter stimulates thickening of its myelin sheath, which is associated with the elongation of the internodal segment and a consequent increase in the saltatory conduction velocity of the nerve impulse.[20,56] Therefore, these results elucidated that a significantly superior remyelination was found after the EV therapy, indicating that the successful peripheral nerve regeneration resulted from the EV therapy.

Consistent with the successful anatomical regeneration, after 28 days of nerve crushed injury, promising signs were shown in the rats with EV therapy to reestablish functional recovery, as assessed by the behavioral tests depicted in Fig. 5a, b and Fig. S4a.† Confirmed by the Hargreaves test with latency analysis, an almost full recovery of sensory function in the QDs-Glu-EV group was observed, showing an obvious tendency of returning to the pre-injury level at 28 d post-injury compared with the QDs-Glu group. Most importantly, the rats treated with QDs-Glu-EVs demonstrated a significantly shorter plantar test reaction time at 28 d post-injection than those injected with QDs-Glu regarding temperature sensation ($P = 0.0432$) (Fig. 5d). However, no significant difference was found regarding pain sensation (Fig. S4b†), indicating a slower pain

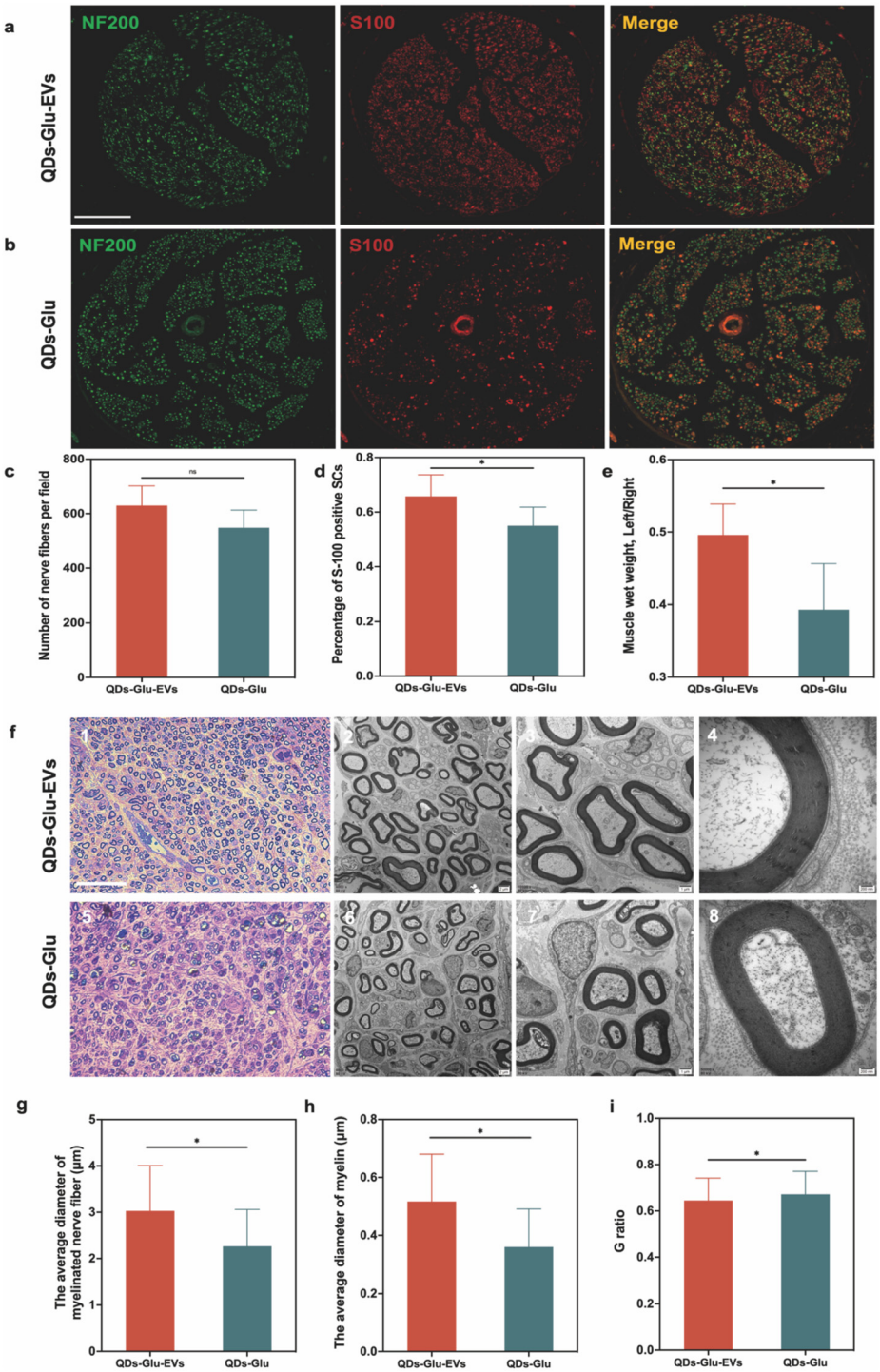

Fig. 4 Peripheral nerve regeneration of the injured sciatic nerve from rat models with and without EV therapy. Representative immunofluorescence staining images with neurofilaments (NF200, green) and SCs (S100, red), and stained and merged images (yellow) (scale bars represent 100 μm) of (a) the QDs-Glu-EV group and (b) the QDs-Glu group. (c) Number of nerve fiber calculation, (d) percentage of S100 positive SCs and (e) muscle wet weight between the QDs-Glu-EV group and the QDs-Glu group. (f1) and (f5) Toluidine blue staining (scale bars represent 50 μm) and (f2–f4) and (f6–f8) TEM images of the myelination of the peripheral nerve fiber in the QDs-Glu-EV group and the QDs-Glu group. (g) Diameter of the myelinated nerve fiber, (h) diameter of myelin and (i) *G* ratio between QDs-Glu-EV group and the QDs-Glu group.

sensation recovery than that of temperature sensation. Furthermore, the rats treated with QDs-Glu-EVs demonstrated significantly higher sciatic functional index (SFI) scores at 21 d (P = 0.0401) and 28 d (P < 0.0001) post-injection than those injected with QDs-Glu (Fig. 5c, e and Fig. S5†), illustrating a superior recovery of neural function after the EV therapy.

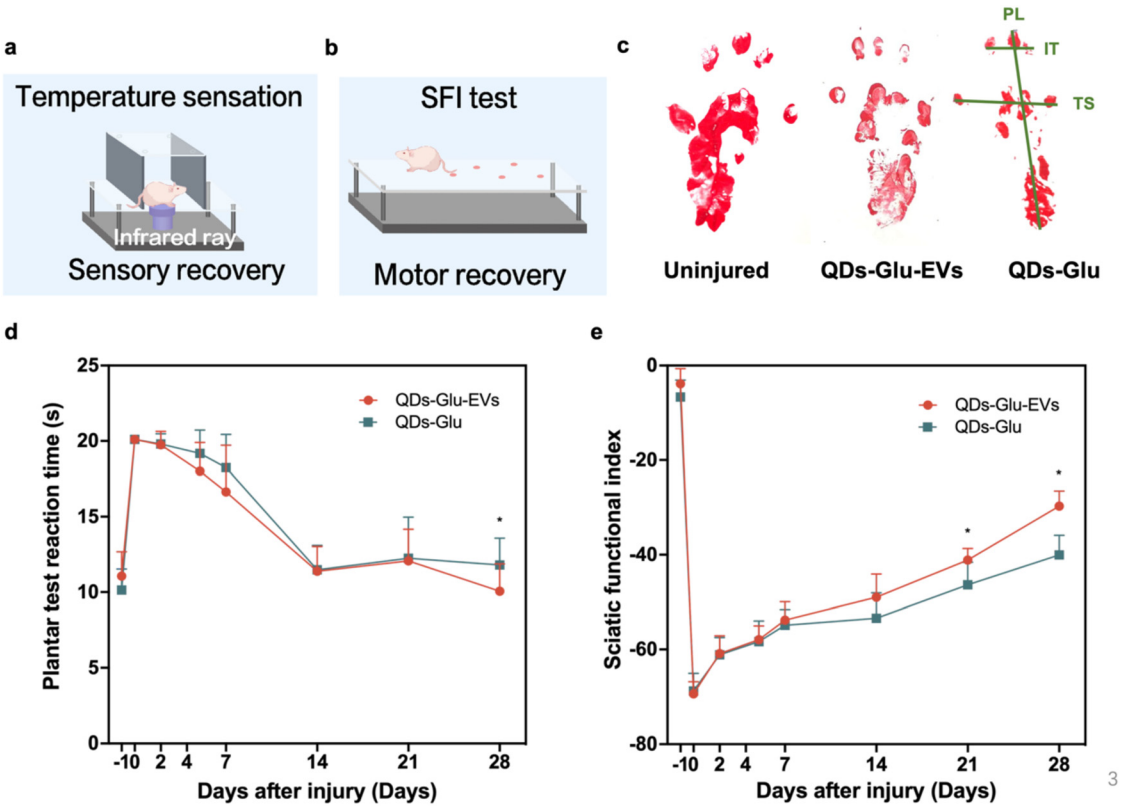

Fig. 5 Behavioral tests of functional recovery in rat models of sciatic nerve injury with and without EV therapy. Schematic illustration of (a) sensory recovery based on temperature sensation, (b) motor recovery based on the SFI test of rats between the QDs-Glu-EV group and the QDs-Glu group. (c) SFI picture of rats in the uninjured rats, the QDs-Glu-EV group and the QDs-Glu group at 28 d post-injury. (d) Plantar test reaction time and (e) SFI test of rats after injury between the QDs-Glu-EV group and the QDs-Glu group.

A variety of newly emerging therapies for PNI mainly including neural tissue engineering focusing on different types of nerve guide conduits and cell therapies using mesenchymal stem cells (MSCs) or EVs.[57–60] SKP-SCs were recently demonstrated to benefit the recovery of spinal cord injury and improve the behavioral recovery in rats with acute and delayed PNI, especially PNI with motor dysfunction.[10,20] SKP-SC-EV treatment was reported to be a novel promising strategy with a pronounced therapeutic potential for improving the axonal outgrowth and regeneration of motoneurons, in which study transection of the sciatic nerve due to crush injury in rats was effectively repaired by treatment with SKP-SC-EVs.[20] Theoretically, the successful transfer of EVs into target cells would provide RNA, protein, and lipids,[61] although the information reservoir of SKP-SC-EVs has not been identified yet. Nevertheless, the current results suggested that these rats with injected SKP-SC-EVs regained functional recovery with superior motor recovery than sensory recovery at an earlier time of 28 d post-injection.

In short, the special therapeutic effects on the motor recovery of SKP-SC-EV therapy were verified, along with a recovery time of 28 days at an EV concentration of 5×10^7 EVs, demonstrating the major factors of the pharmacodynamics of EV therapy under the circumstances. Most importantly, the functional recovery could be reflected by a specific NIR-II fluorescence imaging pattern in the current work, which might possibly realize the real-time dynamic prediction of peripheral nerve regeneration in future.

The major organs of the rats in the QDs-Glu-EV group and the QDs-Glu group were harvested at 4 weeks post-injection to study the biosafety of QDs-Glu-EVs. The bright field photographs of freshly dissected organs are shown in Fig. 6a1 and b1, and no obvious abnormality was discovered. As shown in Fig. 6a2 and b2, most of the organs, including brain, cerebellum, heart, liver, spleen, lungs, kidneys and nerve showed subtle NIR-II fluorescence signals, indicating the clearance of injected QDs-Glu-EVs and QDs-Glu out of the body. Interestingly, it was worth noting that the signals detected in the kidneys ($P < 0.0001$), liver ($P < 0.0001$) and spleen ($P = 0.0023$) were significantly lower in the QDs-Glu-EV group than that of the QDs-Glu group, while in the nerve were significantly higher ($P < 0.0001$) (Fig. 6c). Regarding the previous studies,[37,62] the QDs mainly were metabolized through the liver and excreted through the kidneys and the digestive tract, which agreed with the current results. Furthermore, the relationship between signals in the metabolic organs and the nerve indicated a longer retention of QDs-Glu-EVs in the injured nerve than purely QDs-Glu, which drew a spatio-temporal picture of retention, metabolism and excretion of the injected EVs. In addition, the biosafety was further testified by

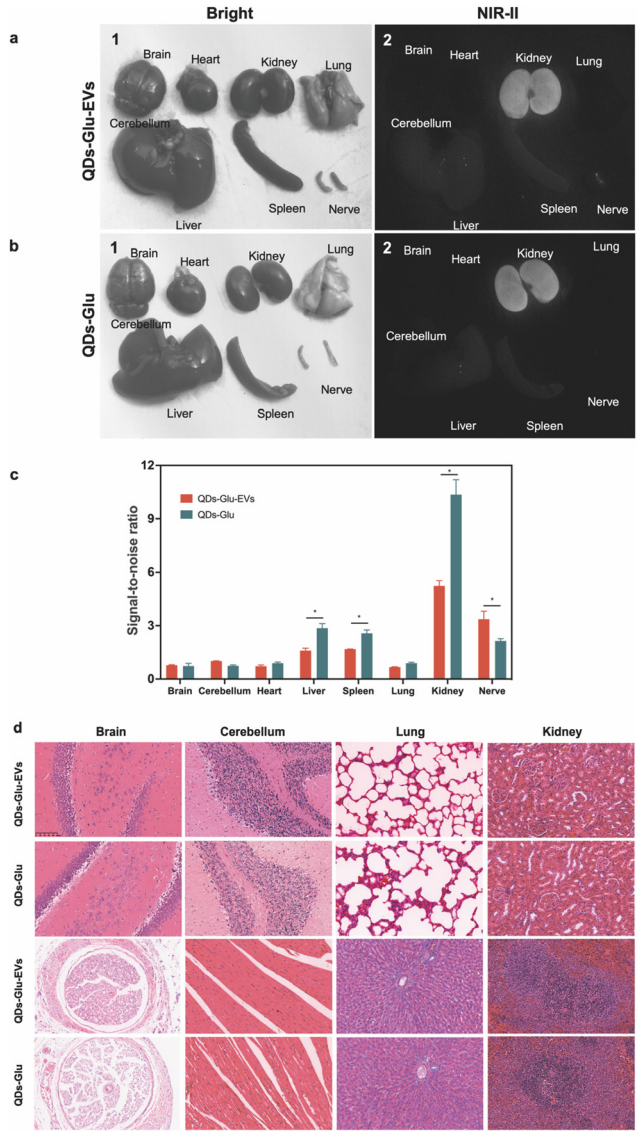

Fig. 6 Biosafety of EV therapy based on QDs-Glu-EVs. (a1 and b1) Bright field photographs and (a2 and b2) NIR-II fluorescence images of the major organs harvested from the rats in the QDs-Glu-EV group and the QDs-Glu group at 4 weeks post-injection. (c) PL intensity analyzed from (a2 and b2). (d) Representative H.E. staining of the major organs collected from the rats in the QDs-Glu-EV group and the QDs-Glu group at 4 weeks post-injection (scale bars represent 100 μm).

hematoxylin and eosin (H.E.) staining (Fig. 6d). The representative images demonstrated major organs collected at 4 weeks post-injection from the rats injected with QDs-Glu-EVs in comparison with QDs-Glu. No noticeable injury or inflammation was observed, which further ensured the biosafety of EV therapy.

Conclusions

In this study, *in vivo* dynamic monitoring of SKP-SC-EVs based on NIR-II fluorescence imaging during sciatic nerve regeneration was successfully achieved. By labeling EVs with QDs, accurate, reliable and real-time records of the migration, distribution, metabolism and excretion *in vivo* were obtained, and the therapeutic effects of EV therapy in peripheral nerve regeneration were confirmed. The *in vivo* results demonstrated that the NIR-II fluorescence signals of QDs-Glu-EVs in the uninjured site of the crushed nerve decreased steadily accompanied by a gradual increase in the injured site during the 21-day observation, indicating the migration of EVs from the injected site of the nerve to the injured site, and then the possibly released contents from 4 d to 7 d post-injection. The histological analysis demonstrated remyelination during enhanced nerve regeneration with EV therapy. The behavioral tests showed nerve functional recovery when EVs were administered, especially the motor recovery at 28 d post-injection. The mapping relationship between functional recovery and the NIR-II fluorescence imaging change pattern was decoded and depicted. Our findings indicated that sciatic nerve injury treated with the SKP-SC-EV therapy resulted in nerve regeneration and neurofunctional recovery, the process of which could be precisely deciphered by NIR-II fluorescence imaging *in vivo*, displaying considerable potential for future PNI treatment under real-time monitoring.

Ethics

This work received the approval of Ethics by the Ethics Committee of Fudan University (201903001S).

Consents for publication

Consents for publication were received from all authors.

Author contributions

Yueming Wang: conceptualization, methodology, and writing – review and editing; Huaixuan Sheng: validation, resources, investigation, and writing – review and editing; Meng Cong: methodology, software, and formal analysis; Wenjin Wang: data curation, formal analysis, and conceptualization; Qianru He: resources, data curation, and formal analysis; Huizhu Li: resources, data curation, and investigation; Shunyao Li: resources and investigation; Jian Zhang: data curation and formal analysis. Yuzhou Chen: formal analysis; Shuaicheng Guo: software; Lu Fang: software and visualization; Stefano Pluchino: conceptualization; Ewelina Biskup: conceptualization; Mikhail Artemyev: supervision; Fuchun Chen: supervision; Yunxia Li: project administration; Jun Chen: supervision, project administration, and funding acquisition; Sijia Feng: original draft, review and editing, and project administration; and Yan Wo: supervision, project administration, and funding acquisition.

Conflicts of interest

The authors declare no interest conflict.

Acknowledgements

The authors thank Hao Chen and his team from Shanghai Institute of Materia Medica, Chinese Academy of Sciences for providing the NIR-II imaging instrument. This work was supported by the Shanghai Science and Technology Development Foundation (21ZR1436100), the National Natural Science Foundation of China (82072521, 82011530023 and 82111530200), the Shanghai Talent Development Funding Scheme (2020080), the Shanghai Sailing Program (22YF1405200 and 23YF1404300), the Shanghai Committee of Science and Technology (22DZ2204900, 23ZR1445700), and the Medical Engineering Joint Fund of Fudan University (YG2022-14).

References

1 M. Asplund, M. Nilsson, A. Jacobsson and H. von Holst, *Neuroepidemiology*, 2009, **32**, 217–228.
2 G. R. Evans, *Anat. Rec.*, 2001, **263**, 396–404.
3 C. A. Taylor, D. Braza, J. B. Rice and T. Dillingham, *Am. J. Phys. Med. Rehabil.*, 2008, **87**, 381–385.
4 M. Artico, L. Cervoni, F. Nucci and R. Giuffré, *Neurosurgery*, 1996, **39**, 380–382; discussion 382–383.
5 B. Battiston, I. Papalia, P. Tos and S. Geuna, *Int. Rev. Neurobiol.*, 2009, **87**, 1–7.
6 S. Tang, J. Zhu, Y. Xu, A. P. Xiang, M. H. Jiang and D. Quan, *Biomaterials*, 2013, **34**, 7086–7096.
7 A. Pabari, S. Y. Yang, A. M. Seifalian and A. Mosahebi, *J. Plast., Reconstr. Aesthetic Surg.*, 2010, **63**, 1941–1948.
8 G. Lundborg, *J. Hand Surg., Am. Vol.*, 2000, **25**, 391–414.
9 M. Sakuma, G. Gorski, S. H. Sheu, S. Lee, L. B. Barrett, B. Singh, T. Omura, A. Latremoliere and C. J. Woolf, *Eur. J. Neurosci.*, 2016, **43**, 451–462.
10 H. T. Khuong, R. Kumar, F. Senjaya, J. Grochmal, A. Ivanovic, A. Shakhbazau, J. Forden, A. Webb, J. Biernaskie and R. Midha, *Exp. Neurol.*, 2014, **254**, 168–179.
11 J. S. Sparling, F. Bretzner, J. Biernaskie, P. Assinck, Y. Jiang, H. Arisato, W. T. Plunet, J. Borisoff, J. Liu, F. D. Miller and W. Tetzlaff, *J. Neurosci.*, 2015, **35**, 6714–6730.
12 P. Mehrotra, G. Tseropoulos, M. E. Bronner and S. T. Andreadis, *Stem Cells Transl. Med.*, 2020, **9**, 328–341.
13 C. P. Lai, O. Mardini, M. Ericsson, S. Prabhakar, C. Maguire, J. W. Chen, B. A. Tannous and X. O. Breakefield, *ACS Nano*, 2014, **8**, 483–494.
14 H. Jing, X. He and J. Zheng, *Transl. Res.*, 2018, **196**, 1–16.
15 B. Giebel and D. M. Hermann, *Ann. Transl. Med.*, 2019, **7**, 188.
16 A. V. Vlassov, S. Magdaleno, R. Setterquist and R. Conrad, *Biochim. Biophys. Acta*, 2012, **1820**, 940–948.
17 S. Jia, D. Zocco, M. L. Samuels, M. F. Chou, R. Chammas, J. Skog, N. Zarovni, F. Momen-Heravi and W. P. Kuo, *Expert Rev. Mol. Diagn.*, 2014, **14**, 307–321.
18 G. Raposo and W. Stoorvogel, *J. Cell Biol.*, 2013, **200**, 373–383.
19 H. Valadi, K. Ekström, A. Bossios, M. Sjöstrand, J. J. Lee and J. O. Lötvall, *Nat. Cell Biol.*, 2007, **9**, 654–659.
20 X. Wu, L. Wang, M. Cong, M. Shen, Q. He, F. Ding and H. Shi, *Ann. Transl. Med.*, 2020, **8**, 1640.
21 S. R. Baglio, D. M. Pegtel and N. Baldini, *Front. Physiol.*, 2012, **3**, 359.
22 H. Xin, Y. Li, Y. Cui, J. J. Yang, Z. G. Zhang and M. Chopp, *J. Cereb. Blood Flow Metab.*, 2013, **33**, 1711–1715.
23 H. Xin, Y. Li, B. Buller, M. Katakowski, Y. Zhang, X. Wang, X. Shang, Z. G. Zhang and M. Chopp, *Stem Cells*, 2012, **30**, 1556–1564.
24 A. D. Pusic and R. P. Kraig, *Glia*, 2014, **62**, 284–299.
25 L. Hu, S. A. Wickline and J. L. Hood, *Magn. Reson. Med.*, 2015, **74**, 266–271.
26 X. Zhao, H. Zhao, Z. Chen and M. Lan, *J. Nanosci. Nanotechnol.*, 2014, **14**, 210–220.
27 P. K. Nguyen, J. Riegler and J. C. Wu, *Cell Stem Cell*, 2014, **14**, 431–444.
28 C. Li, Y. Zhang, M. Wang, Y. Zhang, G. Chen, L. Li, D. Wu and Q. Wang, *Biomaterials*, 2014, **35**, 393–400.
29 G. Chen, I. Roy, C. Yang and P. N. Prasad, *Chem. Rev.*, 2016, **116**, 2826–2885.
30 H. Wan, J. Yue, S. Zhu, T. Uno, X. Zhang, Q. Yang, K. Yu, G. Hong, J. Wang, L. Li, Z. Ma, H. Gao, Y. Zhong, J. Su, A. L. Antaris, Y. Xia, J. Luo, Y. Liang and H. Dai, *Nat. Commun.*, 2018, **9**, 1171.
31 G. Hong, S. Diao, A. L. Antaris and H. Dai, *Chem. Rev.*, 2015, **115**, 10816–10906.
32 K. Welsher, S. P. Sherlock and H. Dai, *Proc. Natl. Acad. Sci. U. S. A.*, 2011, **108**, 8943–8948.
33 Y. Yang, J. Chen, X. Shang, Z. Feng, C. Chen, J. Lu, J. Cai, Y. Chen, J. Zhang, Y. Hao, X. Yang, Y. Li and S. Chen, *Adv. Sci.*, 2019, **6**, 1901018.
34 S. Dong, S. Feng, Y. Chen, M. Chen, Y. Yang, J. Zhang, H. Li, X. Li, L. Ji, X. Yang, Y. Hao, J. Chen and Y. Wo, *Front. Chem.*, 2021, **9**, 676928.
35 O. Betzer, N. Perets, A. Angel, M. Motiei, T. Sadan, G. Yadid, D. Offen and R. Popovtzer, *ACS Nano*, 2017, **11**, 10883–10893.
36 N. Perets, O. Betzer, R. Shapira, S. Brenstein, A. Angel, T. Sadan, U. Ashery, R. Popovtzer and D. Offen, *Nano Lett.*, 2019, **19**, 3422–3431.
37 Y. Kong, J. Chen, H. Fang, G. Heath, Y. Wo, W. Wang, Y. Li, Y. Guo, S. D. Evans, S. Chen and D. Zhou, *Chem. Mater.*, 2016, **28**, 3041–3050.
38 J. A. Biernaskie, I. A. McKenzie, J. G. Toma and F. D. Miller, *Nat. Protoc.*, 2006, **1**, 2803–2812.
39 Y. Lei, H. Tang, L. Yao, R. Yu, M. Feng and B. Zou, *Bioconjugate Chem.*, 2008, **19**, 421–427.
40 K. Hargreaves, R. Dubner, F. Brown, C. Flores and J. Joris, *Pain*, 1988, **32**, 77–88.

41 G. Chen, F. Tian, Y. Zhang, Y. Zhang, C. Li and Q. Wang, *Adv. Funct. Mater.*, 2014, **24**, 2481–2488.
42 C. Landes, M. Braun, C. Burda and M. A. El-Sayed, *Nano Lett.*, 2001, **1**, 667–670.
43 W. G. J. H. M. van Sark, P. L. T. M. Frederix, D. J. Van den Heuvel, H. C. Gerritsen, A. A. Bol, J. N. J. van Lingen, C. de Mello Donegá and A. Meijerink, *J. Phys. Chem. B*, 2001, **105**, 8281–8284.
44 N. Myung, Y. Bae and A. J. Bard, *Nano Lett.*, 2003, **3**, 747–749.
45 S. K. Sarkar, N. Chandrasekharan, S. Gorer and G. Hodes, *Appl. Phys. Lett.*, 2002, **81**, 5045–5047.
46 C. Zhao, X. Wang, L. Wu, W. Wu, Y. Zheng, L. Lin, S. Weng and X. Lin, *Colloids Surf., B*, 2019, **179**, 17–27.
47 L. Pan, S. Sun, A. Zhang, K. Jiang, L. Zhang, C. Dong, Q. Huang, A. Wu and H. Lin, *Adv. Mater.*, 2015, **27**, 7782–7787.
48 Y. Kong, J. Chen, F. Gao, W. Li, X. Xu, O. Pandoli, H. Yang, J. Ji and D. Cui, *Small*, 2010, **6**, 2367–2373.
49 M. Cong, M. Shen, X. Wu, Y. Li, L. Wang, Q. He, H. Shi and F. Ding, *Stem Cell Res. Ther.*, 2021, **12**, 80.
50 S. Gurung, D. Perocheau, L. Touramanidou and J. Baruteau, *Cell Commun. Signaling*, 2021, **19**, 47.
51 R. Kalluri and V. S. LeBleu, *Science*, 2020, **367**(6478), eaau6977.
52 S. Salunkhe, Dheeraj, M. Basak, D. Chitkara and A. Mittal, *J. Controlled Release*, 2020, **326**, 599–614.
53 G. Terenghi, *J. Anat.*, 1999, **194**(Pt 1), 1–14.
54 J. W. Fawcett and R. J. Keynes, *Annu. Rev. Neurosci.*, 1990, **13**, 43–60.
55 Z. L. Chen, W. M. Yu and S. Strickland, *Annu. Rev. Neurosci.*, 2007, **30**, 209–233.
56 Y. Ma, L. Dong, D. Zhou, L. Li, W. Zhang, Y. Zhen, T. Wang, J. Su, D. Chen, C. Mao and X. Wang, *J. Cell. Mol. Med.*, 2019, **23**, 2822–2835.
57 K. Liu, L. Yan, R. Li, Z. Song, J. Ding, B. Liu and X. Chen, *Adv. Sci.*, 2022, **9**, e2103875.
58 J. Ding, J. Zhang, J. Li, D. Li, C. Xiao, H. Xiao, H. Yang, X. Zhuang and X. Chen, *Nano Res.*, 2019, **90**, 1–34.
59 X. Zhang, W. Qu, D. Li, K. Shi, R. Li, Y. Han, E. Jin, J. Ding and X. Chen, *Adv. Mater. Interfaces*, 2020, **7**, 2000225.
60 Y. Han, X. Li, Y. Zhang, Y. Han, F. Chang and J. Ding, *Cells*, 2019, **8**, 886.
61 T. Skotland, K. Sagini, K. Sandvig and A. Llorente, *Adv. Drug Delivery Rev.*, 2020, **159**, 308–321.
62 Z. Feng, Y. Yang, J. Zhang, K. Wang, Y. Li, H. Xu, Z. Wang, E. Biskup, S. Dong, X. Yang, Y. Hao, J. Chen and Y. Wo, *Nano Res.*, 2019, **12**, 3059–3068.